Research Square

Preprints are preliminary reports that have not undergone peer review.
They should not be considered conclusive, used to inform clinical practice,
or referenced by the media as validated information.

Small and Large Glioblastoma Extracellular Vesicles Differentially Regulate Endothelial and Mitochondrial Function in Blood–Brain Barrier and Peripheral Vasculature Models

Deimantė Kulakauskienė
Lithuanian University of Health Sciences
Karolina Kriaučiūnaitė
Lithuanian University of Health Sciences
Zbigniev Balion
Lithuanian University of Health Sciences
Edgaras Stankevičius
Lithuanian University of Health Sciences
Aistė Jekabsone
aiste.jekabsone@lsmu.lt
Lithuanian University of Health Sciences

Research Article

Keywords: glioblastoma, extracellular vesicles, BBB and peripheral endothelium, endothelial bioenergetics

Posted Date: March 3rd, 2026

DOI: https://doi.org/10.21203/rs.3.rs-8945272/v1

License: This work is licensed under a Creative Commons Attribution 4.0 International License. Read Full License

Additional Declarations: No competing interests reported.

Version of Record: A version of this preprint was published at Journal of Neuro-Oncology on April 14th, 2026. See the published version at https://doi.org/10.1007/s11060-026-05555-x.

Abstract

Purpose.

Extracellular vesicles (EVs) released by glioblastoma (GBM) cells circulate systemically and modulate tumour-host interactions, influencing vascular function both within and beyond the tumour microenvironment. The EVs span a size range from tens to hundreds of nanometres; however, the specific effects of distinct GBM-derived EV size subpopulations on endothelial function across different endothelial cell types remain poorly understood.

Methods.

In this study, we investigated the effects of GBM human cell line HROG36-derived small EVs (sEV) and large EVs (lEV) on barrier integrity (transendothelial electrical resistance (TEER) and tight junction (TJ) protein analysis), migration (wound healing assay), angiogenic capacity (tube formation on extracellular matrix), and mitochondrial respiration (MitoStress assay) in human brain microvascular endothelial cells hCMEC/D3 and peripheral endothelial cells HUVECs.

Results.

We show that sEV significantly impaired endothelial barrier integrity in both cell types, as evidenced by reduced TEER and disrupted TJ protein organisation. In contrast, lEV enhanced endothelial cell migration while suppressing angiogenic network formation, resulting in disorganized, shortened capillary-like structures. These functional alterations were accompanied by cell-type- and EV-size-specific changes in mitochondrial respiration, with sEV predominantly reducing bioenergetic capacity, whereas lEV primarily affected mitochondrial function in brain endothelial cells.

Conclusion.

Our data indicate that size-defined GBM-derived EV subpopulations exert distinct vascular effects, providing a rationale for EV size-based biomarkers and personalised therapeutic approaches in GBM.

INTRODUCTION

Cancer cells secrete a complex secretome that readily enters the circulation and induces systemic alterations. Within this secretome, EVs are increasingly recognised as major mediators of long-range intercellular communication, accounting for many of the biological effects observed at sites distant from the tumour. EVs are lipid bilayer-enclosed particles released into the extracellular space and biological fluids [1, 2]. They transport complex molecular cargo, including proteins, lipids, and nucleic acids, and thereby enable

cells to influence the behaviour of distant targets [3–5]. In cancer, EVs are now viewed as active signalling entities that reshape tissue environments and coordinate pathological processes across organ systems, not only passive by-products of cellular activity [6].

A major challenge in EV research is biological and technical heterogeneity. Cells generate EVs through multiple intracellular pathways [7], but their biogenetic origin cannot be reliably inferred after isolation. Overlapping size distributions, shared molecular markers, and isolation-related artefacts further limit the utility of strictly biogenesis-based classification. To address these limitations, the International Society for Extracellular Vesicles (ISEV) has proposed an operational framework that prioritises physical characteristics and transparent reporting over inferred origin [2]. Within this framework, sEV (< 200 nm) and lEV (> 200 nm) are defined as experimentally tractable subpopulations that allow resolution of size-dependent functional effects. Distinguishing sEV from lEV is therefore biologically meaningful. Molecular profiling studies indicate that tumour cells selectively package bioactive cargo into size-defined EV subpopulations. Cancer-derived lEV are enriched in oncogenic proteins, whereas sEV display distinct miRNA and mRNA profiles [6]. Collectively, this suggests that EV subpopulations function as parallel signalling systems with potentially divergent biological roles, and that bulk EV analysis may obscure subpopulation-specific mechanisms.

The vascular system is a particularly sensitive target of EV-mediated signalling in cancer. Tumour-associated vascular abnormalities occur both locally and systemically, including increased permeability and dysregulated angiogenesis, suggesting broader alterations in endothelial functional state rather than isolated defects. Growing evidence indicates that tumour-derived EVs contribute to these changes by modulating endothelial metabolic programmes [8]. Given their stability in circulation and ability to travel long distances, EVs are well positioned to exert vascular effects beyond the tumour microenvironment.

GBM represents a particularly informative model for studying EV-driven vascular dysfunction. As one of the most highly vascularised human tumours, GBM is characterised by profound disruption of the blood–brain barrier (BBB), resulting in a heterogeneous blood–tumour barrier that contributes substantially to disease-associated morbidity and mortality [9–11]. Importantly, GBM-derived EVs are detectable both within the tumour microenvironment and in the peripheral circulation [12], where they are associated with systemic vascular abnormalities, including pro-thrombotic states [13]. These features position GBM as a highly relevant model for investigating EV-mediated vascular effects across central and peripheral compartments.

Despite increasing recognition of the role of GBM-derived EVs in vascular pathology, how distinct size-defined EV subpopulations differentially affect endothelial function remains insufficiently characterised. Most studies rely on bulk EV preparations or focus

predominantly on sEV-enriched isolates, limiting the ability to resolve size-dependent effects on vascular behaviour. Furthermore, potential links between EV-induced endothelial dysfunction and endothelial metabolic state remain largely unexplored. To address these gaps, we performed a subpopulation-resolved analysis of GBM-derived EVs, explicitly distinguishing sEV from lEV. We systematically assessed their effects on endothelial barrier properties, migration, angiogenesis, and metabolic status using both BBB and peripheral endothelial models under matched experimental conditions.

MATERIALS AND METHODS

Cell Lines and Culture Conditions

In this study, we used the immortalised human GBM cell line HROG36 (obtained from CLS Cell Lines Service GmbH, Germany), human umbilical vein endothelial cells (HUVECs; obtained from Thermo Fisher Scientific, USA), and the immortalised human cerebral microvascular endothelial cell line hCMEC/D3 (obtained from Sigma-Aldrich). All commercial cells were maintained in plastic cultureware at 37°C in a humidified incubator with 5% CO□. The culture medium was replaced twice weekly. For subculturing, cells were rinsed once with phosphate-buffered saline (PBS), detached with a 0.05% trypsin-1 mM ethylenediaminetetraacetic acid (EDTA) solution (Gibco), resuspended in fresh medium, and then transferred to new culture flasks for continued growth.

For expansion before the EV collection, HROG36 cells were grown in Dulbecco's Modified Eagle Medium/Nutrient Mixture F-12 (DMEM/F-12; Gibco), supplemented with 10% fetal bovine serum (FBS; Gibco) and 1% penicillin–streptomycin (Gibco). The cells used for EV collection were between passages 20 and 35.

All cultureware used for HUVECs was coated with 0.1% gelatin (Sigma-Aldrich, porcine skin-derived), diluted in distilled water, and incubated at 37°C for at least 30 minutes. HUVECs were grown in endothelial cell growth medium (ECGM; Gibco) supplemented with 1x Large Vessel Endothelial Supplement (LVES; Gibco) and 1% penicillin–streptomycin (Gibco). The cells were used for experiments between passages 3 and 6.

All cultureware for hCMEC/D3 cells was precoated with rat tail collagen type I (Gibco) diluted 1:20 in PBS and incubated at 37°C for at least 1 h. hCMEC/D3 were maintained in EndoGRO-MV complete medium (Merk Millipore) containing EndoGRO basal medium, 5% FBS, L-glutamine (10 mM), EndoGRO-LS supplement (0.2%), heparin sulphate (0.75 U/ml), ascorbic acid (50 µg/ml), hydrocortisone hemisuccinate (1 µg/ml), recombinant human epidermal growth factor (5 ng/ml) and were additionally supplemented with freshly added recombinant human fibroblast growth factor (bFGF; 1 ng/ml; Gibco). hCMEC/D3 cells used for the experiments were between passages 12 and 18.

All human cell lines were routinely screened for mycoplasma contamination every three months using a PCR-based detection kit (PhoenixDx® Mycoplasma Mix) according to the manufacturer's instructions. All tests were negative for mycoplasma throughout the study period.

Collection and Isolation of EVs

HROG36 cells were seeded at 3000 cells/cm□ and cultured for 4 days under standard conditions. Cells were then washed twice with room temperature PBS and subsequently cultured for an additional 3 days in medium containing EV-depleted FBS (Exolitus, Lithuania). Conditioned supernatants were processed at 4°C by sequential centrifugation. Firstly, supernatants were centrifuged at 500 × g for 15 min to remove cellular debris, followed by 10,000 × g for 45 min. The 10,000 × g pellet was washed once in ice-cold PBS and recentrifuged at 10,000 × g for 45 min to obtain the lEV fraction. The remaining supernatant was passed through a 0.22 µm filter and subjected to ultracentrifugation at 167 000 × g for 2 h using a SORVALL WX Ultra Series ultracentrifuge equipped with a T-865 fixed-angle rotor (8 × 36 mL). Pellets were gently resuspended in ice-cold PBS and washed by a second ultracentrifugation at 167 000 × g for 2 h in the same tubes/rotor to obtain the sEV fraction. Final lEV and sEV pellets were resuspended in ice-cold PBS to 1,000× relative to the starting conditioned volume (e.g., EVs from 100 ml resuspended in 100 µl) and stored at -80°C.

Experimental Design

After purifying both EV populations from HROG36, the samples were characterised and used to treat target cells. To evaluate biological effects, HUVECs were seeded at 100,000 cells/cm□ and hCMEC/D3 at 60,000 cells/cm□. After seeding, cells were cultured for 3 days to ensure the establishment of a fully confluent monolayer before treatment. During the experiments, the culture medium was refreshed and supplemented with the designated experimental groups: sEV, lEV, vehicle control (PBS), and positive control (VEGF/bFGF; only for the tube formation assay). EV treatments were standardised by applying equal volumes of each preparation rather than normalising to particle number or total protein content. This approach was intentionally selected to more closely recapitulate the physiological tumour microenvironment, in which cells are exposed to the total secretome produced by tumours of varying sizes and activity levels. By avoiding artificial normalisation, we preserved biologically relevant differences in EV yield, thereby modelling the naturally generated cumulative signalling output of tumours. For functional assays, 1000× concentrated lEV and sEV were applied at a dose of 10 µL/cm□ of culture surface area. Three days post-treatment, functional changes in target cells were assessed.

Cryogenic Transmission Electron Microscopy (cryo-TEM)

Cryo-TEM service for visualisation of sEV and lEV samples was acquired from the Life Science Centre at Vilnius University, Lithuania. Cu300 mesh R1.2/1.3 holey carbon grids (Quantifoil) were utilised for sample preparation. Before analysis, the grids were glow-discharged for 45 seconds at 25 mA with the GloQube Plus system (Quorum Technologies). An aliquot of 3 µL of aqueous EV solution was applied to the carbon side of the grid, blotted for 5.0 seconds, and then plunge-frozen in precooled liquid ethane using the Vitrobot Mark IV (Thermo Fisher Scientific). Embedding the EVs in a thin amorphous ice layer is crucial to preserving their native state and preventing radiation damage. Imaging was performed using a Thermo Fisher Scientific Glacios cryo-electron microscope at 200 kV, equipped with a Falcon 3EC Direct Electron Detector operating in electron-counting mode (Vilnius University, Lithuania). Images were acquired using EPU software (version 2.14.0) at a magnification of 92,000×, yielding a calibrated pixel size of 1.10 Å. The parameters were an exposure rate of 0.81 e/å□/s, a total dose of 29.7 e/å□ per image, and a defocus of -2.0 µm.

Nanoparticle Tracking Analysis (NTA)

The size distribution and quantification of isolated EV samples were analysed using a NanoSight NS300 system (Malvern Panalytical, UK). All samples were diluted in filtered PBS to achieve an optimal particle count per frame (30–100 particles/frame). The camera level and detection threshold were optimised for each sample individually to ensure precise particle detection and tracking. Five 1-min videos were captured with an sCMOS camera and a 488 nm blue laser for each measurement. The videos were then analysed using the NanoSight Software NTA 3.4 Build 3.4.4, with a detection threshold of 5.

Tunable Resistive Pulse Sensing (TRPS)

Additional particle size and concentration analysis of EV samples was performed using the Exoid TRPS measurement system (Izon Science Ltd.) according to the manufacturer’s instructions. An NP100 (C03533) nanopore was used for sEV, and an NP300 (C02615) nanopore for lEV. Samples were diluted 1:100 prior to analysis. The system was calibrated using carboxylated polystyrene calibration particles (CPC200 for sEV and CPC400 for lEV; Izon Science Ltd.) to ensure accurate size and concentration measurements. All measurements were performed under consistent stretch and voltage conditions, and size and concentration were determined by comparing EV blockade signals with those obtained from the calibration particles. Two independent samples for sEV and lEV were measured at three different pressure settings. For data analysis, the size and concentration

distributions from each measurement were exported with a 2 nm bin size, averaged, and the reported values represent the mean of these measurements.

Immunocytochemistry

Endothelial cells were fixed in 4% paraformaldehyde for 20 minutes at room temperature to analyse TJ proteins, then permeabilised with 0.1% Triton X-100 for 15 minutes. After each step, samples were washed three times with PBS at room temperature. They were then blocked with 1% bovine serum albumin for 30 min at room temperature and incubated overnight at 4°C with primary antibodies targeting Zonula occludens-1 (ZO-1; 1:1000; Cell Signaling Technology, Cat. No. 5406) and Claudin-5 (1:1000; Cell Signaling Technology, Cat. No. 66879). The following day, samples were washed thrice with PBS and incubated with Alexa Fluor-conjugated secondary antibodies (1:1000) for 1 h at room temperature in the dark. After a further three PBS washes, nuclei were stained with Hoechst H33342 (Bisbenzimide) for 5 min at room temperature. Imaging was performed using an automated Olympus ApexView 100 fluorescence microscope at 40× magnification.

EV Labelling and Internalisation Assay

Purified EVs were labelled with SYTO™ Green Fluorescent Nucleic Acid Stains (Invitrogen) that bind to RNA within the vesicles. The labelling was performed according to the manufacturer's instructions, using a 10 µM concentration and a 30-min incubation at 37°C in 5% CO□. After incubation, fluorescence intensity was measured using a spectrofluorometer at excitation/emission wavelengths of 490/530 nm, respectively. To remove excess dye, small vesicle fractions were washed using ExoSpin columns, while larger vesicles were centrifuged twice at 10,000×g for 45 minutes at 4°C. The fluorescence was reassessed after washing to confirm dye removal and stability. The labelled EVs were then applied to cells in 35-mm glass-bottom Petri dishes. After 24 h, cells were stained with CellMask™ Plasma Membrane Stain (Invitrogen) at 1×, prepared according to the manufacturer's protocol, for 45 min in the dark, followed by two washes with warm culture medium. Nuclei were stained with Hoechst H33342 (1 µg/mL in PBS) for 5 min at room temperature. Finally, samples were imaged using a Carl Zeiss Axio Observer Z1 fluorescence microscope with a 100× immersion objective, and the images were processed using ImageJ.

Assessment of Cell Migration

Cell migration was assessed using a scratch (wound-healing) assay. After 72 hours of EV treatment, a sterile 200-µl tip was used to carefully scratch the cell monolayer in each

well. Detached cells were rinsed twice with complete growth media. Fresh full media was added, and the cells were incubated under standard conditions. Images of the wound were taken at 0 and 9 hours using a Leica DMi1 light microscope (Germany) at 4x magnification. The wound area was manually traced in the captured images using ImageJ software (version 1.53) to measure the cell-free region. The percentage wound closure was calculated as follows:

$$\text{Wound Closure}(\%) = (W_0 - W_9 / W_0) \times 100$$

where W_0 represents the wound area at 0 h and W_9 at 9 h.

TEER Measurements

To measure TEER, brain endothelial cells hCMEC/D3 were seeded at 6 × 10□ cells/cm□ and human HUVEC at 1 × 105 cells/cm□ on polyester transwell inserts with 0.4 µm pores (BRAND®) placed in 24-well plates and coated with rat tail collagen I (1:20 in PBS, Gibco) for hCMEC/D3 and coated with gelatin I (0.1% in PBS) for HUVEC. hCMEC/D3 cells were cultured in EndoGRO medium until a confluent monolayer formed. HUVEC cultured in ECGM medium supplemented with LVES under the same conditions. Once confluency was reached, the medium in the upper (luminal) compartment was replaced with fresh medium containing sEV or lEV. TEER was measured using the Millicell® ERS-2 Electrical Resistance System (Merck Millipore). Each insert was measured three times at different positions. To calculate TEER (Ω·cm□), the mean resistance of cell-free inserts was subtracted from the mean readings of inserts containing brain endothelial cell monolayers and multiplied by the membrane surface area according to the following formula:

$$\text{TEER} = (R_{cells} - R_{blank}) \times A$$

where R_{cells} represents the resistance of inserts with cells, R_{blank} the resistance of cell-free inserts, and A the effective membrane area. TEER values were expressed as percentages relative to the untreated control cells.

Endothelial Cell Tube Formation Assay

To evaluate angiogenesis in vitro, a 96-well plate was coated with 50 µL of Geltrex (Thermo Fisher) and incubated at 37°C for at least 30 min to allow polymerisation. Following EV treatment, hCMEC/D3 cells were harvested by trypsinisation, resuspended in fresh growth medium, and seeded onto the Geltrex-coated plates at a density of 32,000 cells per well. After 24 h of incubation, tube formation was assessed using a Leica DMi1 light microscope (Germany). Images for quantitative analysis were acquired at 4× magnification. Quantitative analysis of tube formation was performed using ImageJ (version 1.53) with the Angiogenesis Analyser plugin, following the method described by Carpentier et al. [14]. Untreated hCMEC/D3 cells cultured in EndoGRO-MV complete

medium served as the negative control, whereas treatment with 35 ng/mL recombinant human basic fibroblast growth factor (bFGF) was used as the positive control.

HUVECs were cultured under conditions identical to those described for hCMEC/D3 cells, except that wells were coated with GelNest™ extracellular matrix (NEST Scientific, Woodbridge, NJ, USA) instead of Geltrex. HUVECs were seeded at a density of 10,000 cells per well, and tube formation was analysed after 4 hours of incubation. Images for quantitative analysis were acquired at 10× magnification using a Leica DMi1 light microscope (Leica Microsystems, Germany). Treatment with 25 ng/mL recombinant human vascular endothelial growth factor (VEGF) isoform 165 (PeproTech®, USA) was used as the positive control.

Mitochondrial Respiration

Mitochondrial function was assessed using the Seahorse XFp Cell Mito Stress Test (Agilent Technologies, Santa Clara, CA, USA) according to the manufacturer's instructions. hCMEC/D3 cells were seeded at 6 × 10⁴ cells/cm² and HUVECs at 1 × 10⁴ cells/cm² in Seahorse XFp microplates coated with rat tail collagen I (1:20 in PBS, Gibco) for hCMEC/D3 or gelatin I (0.1% in PBS) for HUVECs and cultured until a confluent monolayer was formed, followed by treatment with EVs for 72 h. Prior to the assay, cells were incubated in Seahorse XF assay medium supplemented with 10 mM glucose, 2 mM glutamine, and 1 mM pyruvate at 37°C in a non-CO_2 incubator for 1 h. Oxygen consumption rate (OCR) was measured under basal conditions and following sequential injection of oligomycin (1 µM), trifluoromethoxy carbonylcyanide phenylhydrazone (FCCP; 2 µM for hCMEC/D3 and 3.5 µM for HUVECs), and rotenone/antimycin A (0.5 µM each) to determine basal respiration, ATP production, proton leak, maximal respiration, spare capacity, and non-mitochondrial respiration.

hCMEC/D3 data were normalised to total protein content per well, determined using the Bradford reagent and measured with a multifunctional plate reader (Infinite 200 Pro Nano Plex, Tecan, Männedorf, Switzerland). HUVEC data were normalised to cell number based on nuclear staining. Briefly, cells were stained with Hoechst 33342 (Sigma-Aldrich, St. Louis, MO, USA) for 10 min, and four independent images per well were acquired using a benchtop fluorescence microscope (Olympus APX 100-HCU, Tokyo, Japan) at 20× magnification. Nuclei were quantified automatically using ImageJ (version 1.53), and the average per well was used for normalisation.

Statistical Analysis

Statistical analysis was performed on at least three independent biological experiments. Data are expressed as the mean and standard deviation (SD). The non-parametric Mann-Whitney U test was used to compare two groups. For comparisons involving three or more groups, data were analysed using a non-parametric Kruskal–Wallis test. Two-way ANOVA

was used to assess differences in mitochondrial respiration parameters. All data were analysed using GraphPad Prism® software version 10.4.2 (534) (GraphPad Software, Inc., USA).

RESULTS

Characterisation and Cellular Internalisation of GBM-Derived sEV and lEV in hCMEC/D3 and HUVEC Cells

A combined centrifugation and ultracentrifugation approach was used to isolate EVs of different sizes from the HROG36-conditioned medium. Their physical characterisation included morphological assessment by cryo-TEM and size-distribution analysis using NTA and TRPS. Cryo-TEM imaging confirmed the presence of round, membrane-bound vesicular structures typical of EVs (Fig. 1a). Both sEV and lEV exhibited a well-defined lipid bilayer membrane, consistent with their biological origin. Representative micrographs reveal vesicles with characteristic diameters of approximately 75 nm for sEV and 300 nm for lEV (Fig. 1a). NTA revealed that the majority of sEV ranged from 50 to 150 nm, with a median diameter of 106.5 ± 6.96 nm, whereas lEV ranged from 70 to 250 nm, with a median of 156.0 ± 29.95 nm. TRPS provided complementary sizing, showing that the majority of sEV were distributed within the 100–150 nm range, with a mode diameter of 113.0 ± 5.1 nm, whereas lEV were predominantly detected between 150 and 400 nm, with a mode diameter of 184.2 ± 14.5 nm. Both methods confirmed the reproducibility of isolation and measurement across replicates (Fig. 1b–c). Despite overall agreement in size trends of HROG36-derived sEV and lEV subpopulations, methodological differences influenced both the detected size range and particle concentration. NTA, which determines particle size based on Brownian motion and light scattering, is particularly sensitive to small, highly diffusive vesicles and therefore captured a relatively large proportion of particles below 100 nm, albeit within a more limited upper detection range for larger lEV subpopulations. In contrast, TRPS, which measures individual particles passing through a calibrated nanopore, detected a broader and more polydisperse population extending up to ~ 1 µm. This broader detection range was reflected in higher size heterogeneity in lEV samples, as indicated by a d90/d10 ratio of ~ 3.0–3.1, compared with ~ 1.6–1.8 for sEV. Methodological differences also influenced the measured particle concentration. Relative to TRPS, NTA reported higher particle concentrations by approximately 2.21-fold for sEV ($2.22 \times 10^{□□}$ vs $1.00 \times 10^{□□}$ particles/ml) and 3.97-fold for lEV ($1.36 \times 10^{□□}$ vs $3.43 \times 10^{□}$ particles/ml; data not shown). Based on these concentration values, a 10 µl dose of each EV preparation used for functional assays corresponded to approximately $10^{□}$ sEV/cm$^{□}$ and $10^{□}$–$10^{□}$ lEV/cm$^{□}$, depending on the analytical method used, with NTA consistently reporting higher particle numbers than TRPS. Importantly,

these discrepancies most likely reflect technical differences in detection principles and sensitivity across size ranges rather than true biological variation between the EV preparations. Thus, NTA and TRPS should be considered complementary rather than conflicting approaches, each providing distinct but supportive information on EV size distribution and concentration. Accordingly, functional treatments were intentionally standardised by preparation volume rather than particle count, thereby ensuring experimental consistency and preventing bias arising from platform-dependent particle quantification variability. Additionally, by applying sEV and lEV isolated from the same initial conditioned medium volume rather than adjusting treatments according to measured particle concentration, we more closely mimic physiological conditions in which EV subpopulations are naturally present in their relative proportions.

A fluorescence-based assay was performed to confirm active EV internalisation by endothelial cells and to visualise their subcellular localisation. After 24 h of incubation, both sEV and lEV were internalised by hCMEC/D3 and HUVEC cells. As shown in Fig. 1d, hCMEC/D3 internalised fluorescently labelled sEVs, exhibiting a fine reticular cytoplasmic pattern. In contrast, lEV in hCMEC/D3 displayed a more diffuse cytoplasmic distribution, suggesting distinct internalization or trafficking routes. In HUVECs, fluorescence imaging also revealed distinct internalisation patterns for sEV and lEV. Following sEV treatment, the fluorescent signal in HUVEC cells was diffusely distributed throughout the cytoplasm without distinct compartmental boundaries, indicating widespread cytosolic localization. By comparison, lEV exposure resulted in fluorescence localized to distinct, vesicular structures reminiscent of endosomes, consistent with retention within membrane-bound intracellular compartments (Fig. 1e).

sEV-Induced Changes in TEER and Tight Junctions

To evaluate the functional and biological effects of EVs on endothelial behaviour, measurements were performed after 72 h, allowing sufficient time for internalised vesicles to elicit measurable responses. TEER was chosen as the primary assay for this purpose, as it provides a direct, quantitative, and real-time measure of barrier integrity, offering immediate insight into cell-cell junction status and overall endothelial functionality, and guiding subsequent in-depth analyses. TEER analysis revealed that sEV treatment reduced barrier integrity in both endothelial cell models. In hCMEC/D3 cells, sEV decreased TEER by $36.79 \pm 22.00\%$ compared with control, while lEV caused a smaller, non-significant decrease of $19.30 \pm 6.70\%$ (Fig. 2a). Similarly, in HUVECs, sEV reduced TEER by $34.13 \pm 9.53\%$, whereas lEV induced a non-significant decrease of $18.95 \pm 10.71\%$ (Fig. 2b). These data indicate that sEV exert a stronger disruptive effect on endothelial barrier function, whereas lEV have little to no impact on barrier integrity.

Following significant TEER changes, immunocytochemistry was performed to visualize key TJ proteins, including Claudin-5 and ZO-1, linking functional barrier disruption to specific

molecular alterations. Fluorescence microscopy revealed distinct effects of EVs on TJ proteins in both endothelial models. In hCMEC/D3 cells, ZO-1 staining showed fragmented and irregular junctional distribution in both sEV- and lEV-treated groups, while Claudin-5 localization was continuous in control cells but disrupted and discontinuous following EV exposure, most prominently after sEV treatment (Fig. 2c). In HUVECs, control cells displayed continuous membrane-associated localization of ZO-1 and Claudin-5, forming a coherent junctional network. Exposure to sEV resulted in diffuse ZO-1 signal throughout the cytoplasm and intense Claudin-5 localization to filopodia, reducing membrane-associated signal, whereas lEV did not induce notable redistribution of either protein compared to control cells (Fig. 2d).

lEV-Induced Modulation of Endothelial Migration and Angiogenesis

Subsequently, endothelial migration was evaluated to determine whether EVs modulate cell motility independent of barrier disruption. To assess cell migration, a wound healing assay was performed. After 9 h in hCMEC/D3 monolayers, lEV treatment increased the migrated area by $17.40 \pm 6.32\%$ relative to control, whereas sEV exposure produced no significant change (Fig. 3a-b). Similarly, in HUVECs, lEV increased cell motility by $33.03 \pm 10.67\%$, whereas sEV had no significant effect (Fig. 3c-d). These results indicate that lEV selectively promotes endothelial cell migration, whereas sEV does not alter motility in either cell type. Because proliferation was not directly assessed during the 9-h migration window, a minor contribution of cell division to wound closure cannot be fully excluded.

The increase in endothelial motility induced by lEV suggested functional activation; therefore, angiogenic potential was subsequently examined to determine whether enhanced migration translates into coordinated vascular network formation. Endothelial angiogenic potential was assessed by measuring the cell ability to form capillary-like tubular structures on an extracellular matrix. Quantitative analysis demonstrated that lEV treatment impaired angiogenic network complexity in hCMEC/D3 cells, reducing the number of nodes (–$23.76 \pm 3,13\%$) and meshes (–$23.77 \pm 5.11\%$) relative to the bFGF control, whereas sEV had no significant effect (Fig. 3e, g). In HUVECs, a similar effect was observed, with lEV-treated cells showing an even more pronounced reduction in the ability to form organised capillary-like networks compared with VEGF-stimulated positive controls. Microscopic image analysis revealed reductions in the number of nodes ($-45.87 \pm 6.90\%$), meshes ($-55.70 \pm 21.57\%$), segments ($-49.09 \pm 13.94\%$), and junctions ($-44.83 \pm 8.18\%$), accompanied by a decrease in total network length ($-32.07 \pm 2.36\%$). In contrast, sEV treatment did not significantly alter any of the angiogenic parameters. (Fig. 3f, h). These findings indicate that large EVs impair the formation of organised capillary-like networks in both hCMEC/D3 and HUVECs, despite enhancing endothelial cell migration.

EV Size-Dependent Effects on Mitochondrial Respiration

Maintenance of endothelial barrier integrity, migration, and angiogenic network formation are highly energy-dependent processes; therefore, the functional alterations observed across these assays prompted further investigation of cellular metabolism. Mitochondrial respiration was subsequently evaluated to determine whether EV-induced changes in endothelial behavior are associated with alterations in bioenergetic capacity. This was performed using the Seahorse XFp Cell Mito Stress Test, which allows real-time assessment of key mitochondrial parameters. In hCMEC/D3 cells, lEV reduced basal respiration by $26.25 \pm 16.77\%$, ATP production by $49.05 \pm 11.54\%$, and maximal respiration by $32.66 \pm 6.48\%$, indicating a significant impairment of mitochondrial function. This may reflect increased energetic demand associated with enhanced migration, while the simultaneous reduction in tube formation suggests that diminished bioenergetic capacity limits organized network assembly. sEV primarily reduced ATP production ($40.05 \pm 12.33\%$) and maximal respiration ($22.38 \pm 11.10\%$), consistent with their TEER-lowering and TJ-disruptive effects (Fig. 4a). In HUVECs, sEV moderately decreased maximal respiration ($14.54 \pm 5.45\%$) and spare respiratory capacity ($21.40 \pm 8.67\%$), whereas lEV had no effect on mitochondrial activity (Fig. 4b). These results highlight a cell type- and EV size-dependent bioenergetic response, with barrier-destabilizing sEV acting via ATP-dependent mechanisms, and lEV promoting motility while limiting organized angiogenesis in an energy-sensitive manner, particularly in BBB endothelial cells.

DISCUSSION

Our study establishes a comparative framework for analysing EVs across different size ranges while prioritising physiological relevance over artificial equalisation. Rather than normalising treatments to particle number or total protein content, we applied equal relative sample volumes generated using an identical isolation and concentration protocol. This approach preserves intrinsic differences in vesicle yield across fractions and more accurately reflects the cumulative secretory output experienced by recipient cells *in vivo*. Although normalisation facilitates direct quantitative comparisons, it may obscure biologically meaningful differences in secretion dynamics, cargo loading, and biogenesis, and protein-based adjustments may include non-vesicular components. By avoiding such corrections, our design captures the integrated signalling potential of each EV population. The resulting variability in absolute particle counts is therefore interpreted not as a confounding factor but as a biologically relevant parameter contributing to tumour-driven intercellular communication.

Because our experimental design preserved natural differences in EV secretion by avoiding particle normalization, careful characterization of vesicle size and heterogeneity was essential for interpreting functional outcomes. NTA and TRPS, which rely on fundamentally different detection principles, provided complementary insights: NTA is highly sensitive to small, diffusive vesicles but may underestimate larger or polydisperse populations, whereas TRPS accurately captures larger and more heterogeneous vesicles through single-particle, pore-based measurement. In our study, both methods consistently identified distinct small and large EV populations; however, the measured particle concentrations differed, reflecting methodological biases. These findings highlight that EV quantification is method-dependent and underscores the value of combining analytical approaches.

A 24-hour incubation period was established to evaluate the internalization of HROG36-derived EVs, ensuring complete uptake beyond the initial binding and early endocytic stages. Durak-Kozica et al. similarly assessed EV internalization in endothelial cells, including HUVECs, after 24 h, demonstrating that this timeframe allows reliable detection of intracellular accumulation [15]. We demonstrated that in hCMEC/D3 cells after sEV treatment, the fluorescent signal exhibited a reticular cytoplasmic pattern, suggesting targeted routing through the endomembrane system, such as the endoplasmic reticulum or Golgi apparatus, a pathway often utilized by exosomes to bypass lysosomal degradation [16]. Conversely, in HUVECs, the signal appears diffusely distributed, suggesting a less compartmentalized pattern. The uptake pathway of lEV further highlighted the specialized nature of the BBB; while these vesicles were sequestered within endosome-like structures in HUVECs – consistent with classical macropinocytosis [17] – they showed diffuse cytoplasmic dispersion in hCMEC/D3 cells. This suggests that the BBB may facilitate more rapid endosomal escape or alternative membrane fusion for larger cargo to maintain intracellular homeostasis.

Numerous *in vitro* and *in vivo* studies have shown that GBM-secreted factors compromise BBB integrity; however, the specific contributions of distinct EV subpopulations remain unclear. We demonstrate that GBM-derived sEV disrupt endothelial barrier integrity in both BBB and peripheral endothelial models, as reflected by reduced TEER and reorganisation of TJ proteins ZO-1 and Claudin-5. Phenotypically, this aligns with previous reports that GBM EVs increase vascular permeability. Notably, Treps et al. [18] showed that GBM stem cell-derived EVs enhance BBB permeability via semaphorin3A/Neuropilin-1 signalling. However, despite similar barrier-disruptive outcomes, the experimental design and likely mechanisms differ. Treps et al. analysed bulk EV preparations containing both sEV and lEV from a defined GBM stem cell population, focusing on short-term exposure. In contrast, we performed a size-resolved comparison of sEV versus lEV derived from non-stem GBM cultures under prolonged (72 h) treatment and evaluated responses in both BBB and peripheral endothelium. Given that semaphorin3A is primarily associated with a

GBM stem cell phenotype [19], our findings suggest that barrier disruption by non-stem GBM-derived sEV is likely mediated, at least in part, by additional mechanisms beyond semaphorin3A/Neuropilin-1 signalling. Although Treps et al. demonstrated preferential association of semaphorin3A with the exosomal marker CD63, they did not assess the functional effects of this isolated EV subpopulation. Consequently, it remains unclear whether the observed increase in permeability reflects the combined activity of heterogeneous EV populations or the effect of a specific CD63-positive EVs. Our study has a similar limitation: the combined effects of sEV and lEV were not evaluated. Together, these observations indicate that although sEV consistently impair endothelial barriers, the underlying molecular pathways are context- and cell-phenotype-dependent, warranting further compositional and mechanistic analyses of distinct EV subpopulations.

While sEV primarily affected barrier integrity, lEV selectively enhanced endothelial migration in both hCMEC/D3 and HUVEC cells, indicating activation of pro-migratory signalling pathways that are not a consequence of junctional disruption. This observation is in line with a recent study demonstrating that patient-derived GBM lEV promote tumour cell migration via intracellular calcium transients mediated by Connexin-43 gap junctions and subsequent PYK2 phosphorylation [20]. Although these mechanisms were described in the context of tumour cells, they suggest that lEV can promote calcium-dependent motility independently of classical VEGF-VEGFR-dependent angiogenic signalling. A similar signalling axis may shape the endothelial response observed in our study; however, direct investigation of Connexin-43-dependent calcium dynamics and downstream kinases in endothelial cells would be required to confirm this hypothesis.

The VEGF-VEGFR-independent mechanism of migration may further explain why increased motility did not translate into enhanced angiogenesis, as lEV impaired the formation of organised capillary-like networks in vitro. If lEV preferentially activate calcium-dependent pathways, this may promote individual cell movement and inhibit the coordinated network assembly necessary for tube formation. Additionally, another study suggests that EVs and growth factors promote different signalling routes within a tumour, and that their relative contributions may account for clinically relevant differences in vessel morphology and permeability [21]. In this context, endothelial migration and tube formation may not be regulated by the same signalling cascade, and lEV-induced motility and angiogenesis may therefore occur independently of the canonical VEGF pathway.

Importantly, discrepancies with earlier reports may be attributable to differences in EV preparation. In contrast to previous studies that mainly examined bulk EVs or sEV and reported predominantly pro-angiogenic, dose- and time-dependent endothelial activation, our findings indicate a distinct effect of size-resolved fractions. For example, Giusti et al. [22] demonstrated that bulk EV preparations from U251 GBM cells stimulate BBB endothelial proliferation, migration, and tube formation in a dose-dependent manner (2–8

µg/ml), with stronger effects at 72 h compared with earlier time points. Similarly, Yang et al. [23] reported that U251-derived sEV enhance HUVEC migration and tube formation, and Monteforte et al. [24] found that sEV from A-172 increase HUVEC angiogenic activity. However, our size-resolved analysis reveals that lEV can strongly promote endothelial motility while simultaneously impairing organised tube morphogenesis, indicating that different EV fractions can drive distinct and sometimes opposing endothelial programmes.

A key novel contribution of this study is the link between EV-induced functional changes and endothelial mitochondrial bioenergetics. Tumour-derived EVs are increasingly recognized as regulators of metabolic adaptation within the vascular microenvironment [25]. We found that sEV markedly impaired mitochondrial respiration in both hCMEC/D3 and HUVECs, resulting in reduced ATP production and diminished respiratory reserve. Because endothelial barrier maintenance requires continuous ATP-dependent cytoskeletal tension and junctional protein trafficking, energetic insufficiency is expected to preferentially destabilize TJ organization. Similar links between mitochondrial dysfunction and BBB permeability have been suggested in neurovascular disorders [26] but have rarely been explored in the context of tumour-derived EVs. Collectively, these observations indicate that, although mitochondrial suppression itself compromises endothelial barrier integrity, our findings identify GBM-derived EVs as a potential upstream trigger that induces comparable mitochondrial dysfunction and barrier weakening. In contrast, lEV promoted endothelial migration but impaired the formation of organized vascular networks without substantially affecting respiration in HUVECs. This phenotype is consistent with pathological angiogenesis, characterized by increased endothelial motility and aberrant vascular architecture with compromised structural hierarchy and stability, as described in tumour vasculature models [27]. Notably, lEV still suppressed ATP production and maximal respiration in hCMEC/D3, indicating that the metabolically specialized brain endothelium remains vulnerable to mitochondrial perturbation even when the peripheral endothelium is not. Overall, these findings underscore the differential bioenergetic effects of EV subpopulations on endothelial cells and call for deeper investigation into the mechanisms linking mitochondrial modulation to barrier and vascular function.

CONCLUSION

In this study, we demonstrate that GBM-derived EVs exert size-dependent and functionally distinct effects on endothelial biology in both BBB and peripheral vascular models. sEV primarily compromise endothelial barrier integrity, whereas lEV enhance endothelial cell migration across both endothelial cell models while disrupting the formation of organised angiogenic networks. These divergent functional outcomes are accompanied by distinct effects on mitochondrial bioenergetics, with sEV suppressing mitochondrial function in both endothelial models, while lEV induce mitochondrial impairment primarily in the BBB

endothelium. Collectively, our findings establish that sEV and lEV are biologically distinct signalling entities that differentially shape vascular behaviour in GBM. This underscores the importance of size-resolved EV analysis for mechanistic studies and provides a foundation for developing EV-based biomarkers and targeted strategies to mitigate tumour-associated vascular dysfunction.

Abbreviations

• BBB
Blood–Brain Barrier
• bFGF
Basic Fibroblast Growth Factor
• Cryo
TEM–Cryogenic Transmission Electron Microscopy
• ECGM
Endothelial Cell Growth Medium
• EVs
Extracellular Vesicles
• FBS
Fetal Bovine Serum
• FCCP
Trifluoromethoxy Carbonylcyanide Phenylhydrazone
• GBM
Glioblastoma
• lEV
Large Extracellular Vesicles
• LVES
Large Vessel Endothelial Supplement
• NTA
Nanoparticle Tracking Analysis
• OCR
Oxygen Consumption Rate
• PBS
Phosphate–Buffered Saline
• sEV
Small Extracellular Vesicles
• SD
Standard Deviation
• TEER
Transendothelial Electrical Resistance

• TJ
Tight Junction
• TRPS
Tunable Resistive Pulse Sensing
• VEGF
Vascular Endothelial Growth Factor
• ZO
1–Zonula Occludens–1

Declarations

ACKNOWLEDGEMENTS

The authors thank UAB Exolitus for providing access to the NanoSight NS300 and Izon Exoid instruments, which enabled NTA and TRPS analyses for EV characterisation.

AUTHOR CONTRIBUTIONS

D.K. and K.K. contributed equally; A.J., E.S. conceived the idea; D.K., K.K. designed the experiments; D.K., K.K. isolated the EV fractions; D.K. performed and analysed all HUVEC experiments; K.K. performed and analysed HROG36 and hCMEM/D3 experiments; A.J., Z.B. contributed to EV characterisation. D.K., K.K., A.J. wrote the paper. All authors reviewed the manuscript.

FUNDING

This project has received funding from the Research Council of Lithuania (LMTLT), agreement No S-PD-24-107and The Lithuanian University of Health Sciences Research Fund.

DATA AVAILABILITY

The datasets generated during the current study are available from the corresponding author on reasonable request.

COMPETING INTERESTS

The authors have no relevant financial or non-financial interests to disclose.

COMPLIANCE WITH ETHICAL STANDARDS

Ethics approval and consent to participate

This study was conducted using commercially available, previously established human cell lines (HUVEC, HROG36, and hCMEC/D3). No primary human material and no human participants were involved in this study. All methods were carried out in accordance with relevant institutional and national guidelines and regulations. According to institutional policies and applicable regulations, ethical approval and informed consent were not required for the use of established commercial human cell lines.

Consent for publication

Not applicable.

References

1. Welsh JA, Goberdhan DCI, O'Driscoll L, Buzas EI, Blenkiron C, Bussolati B, Cai H, Di Vizio D, Driedonks TAP, Erdbrügger U, Falcon-Perez JM, Fu QL, Hill AF, Lenassi M, Lim SK, Mahoney MG, Mohanty S, Möller A, Nieuwland R, Ochiya T, Witwer KW (2024) Minimal information for studies of extracellular vesicles (MISEV2023): From basic to advanced approaches. J Extracell vesicles 13(2):e12404. https://doi.org/10.1002/jev2.12404
2. Vaiaki EM, Falasca M (2024) Comparative analysis of the minimal information for studies of extracellular vesicles guidelines: Advancements and implications for extracellular vesicle research. Sem Cancer Biol 101:12–24. https://doi.org/10.1016/j.semcancer.2024.04.002
3. Iannotta D, Kijas AA, Rowan AW, A. E., Wolfram J (2024) Entry and exit of extracellular vesicles to and from the blood circulation. Nat Nanotechnol 19(1):13–20. https://doi.org/10.1038/s41565-023-01522-z
4. Verweij FJ, Revenu C, Arras G, Dingli F, Loew D, Pegtel DM, Follain G, Allio G, Goetz JG, Zimmermann P, Herbomel P, Del Bene F, Raposo G, van Niel G (2019) Live Tracking of Inter-organ Communication by Endogenous Exosomes. Vivo Dev cell 48(4):573–589e4. https://doi.org/10.1016/j.devcel.2019.01.004
5. Ye Y, Shi Q, Yang T, Xie F, Zhang X, Xu B, Fang J, Chen J, Zhang Y, Li J (2022) Vivo Visualized Tracking of Tumor-Derived Extracellular Vesicles Using CRISPR-Cas9 System. Technol Cancer Res Treat 21:15330338221085370. https://doi.org/10.1177/15330338221085370
6. Yekula A, Minciacchi VR, Morello M, Shao H, Park Y, Zhang X, Muralidharan K, Freeman MR, Weissleder R, Lee H, Carter B, Breakefield XO, Di Vizio D, Balaj L (2019) Large and small extracellular vesicles released by glioma cells in vitro and in vivo. J Extracell vesicles 9(1):1689784. https://doi.org/10.1080/20013078.2019.1689784

7. Raposo G, Stoorvogel W (2013) Extracellular vesicles: exosomes, microvesicles, and friends. J Cell Biol 200(4):373–383. https://doi.org/10.1083/jcb.201211138
8. Wang B, Wang X, Hou D, Huang Q, Zhan W, Chen C, Liu J, You R, Xie J, Chen P, Huang H (2019) Exosomes derived from acute myeloid leukemia cells promote chemoresistance by enhancing glycolysis-mediated vascular remodeling. J Cell Physiol 234(7):10602–10614. https://doi.org/10.1002/jcp.27735
9. Gargini R, Segura-Collar B, Sánchez-Gómez P (2020) Cellular Plasticity and Tumor Microenvironment in Gliomas: The Struggle to Hit a Moving Target. Cancers 12(6):1622. https://doi.org/10.3390/cancers12061622
10. Naro GR, Noverati N, Craig T (2020) The Role of C1-Esterase Inhibitors in the Management of Vasogenic Edema in Glioblastoma. Case reports in medicine, 2020, 7981609. https://doi.org/10.1155/2020/7981609
11. Arvanitis CD, Ferraro GB, Jain RK (2020) The blood-brain barrier and blood-tumour barrier in brain tumours and metastases. Nat Rev Cancer 20(1):26–41. https://doi.org/10.1038/s41568-019-0205-x
12. García-Romero N, Carrión-Navarro J, Esteban-Rubio S, Lázaro-Ibáñez E, Peris-Celda M, Alonso MM, Guzmán-De-Villoria J, Fernández-Carballal C, de Mendivil AO, García-Duque S, Escobedo-Lucea C, Prat-Acín R, Belda-Iniesta C, Ayuso-Sacido A (2017) DNA sequences within glioma-derived extracellular vesicles can cross the intact blood-brain barrier and be detected in peripheral blood of patients. Oncotarget 8(1):1416–1428. https://doi.org/10.18632/oncotarget.13635
13. Tawil, N., Bassawon, R., Meehan, B., Nehme, A., Montermini, L., Gayden, T., De Jay,N., Spinelli, C., Chennakrishnaiah, S., Choi, D., Adnani, L., Zeinieh, M., Jabado,N., Kleinman, C. L., Witcher, M., Riazalhosseini, Y., Key, N. S., Schiff, D., Grover,S. P., Mackman, N., ... Rak, J. (2021). Glioblastoma cell populations with distinct oncogenic programs release podoplanin as procoagulant extracellular vesicles. Blood advances, 5(6), 1682–1694. https://doi.org/10.1182/bloodadvances.2020002998
14. Carpentier G, Berndt S, Ferratge S, Rasband W, Cuendet M, Uzan G, Albanese P (2020) Angiogenesis Analyzer for ImageJ - A comparative morphometric analysis of Endothelial Tube Formation Assay and Fibrin Bead Assay. Sci Rep 10(1):11568. https://doi.org/10.1038/s41598-020-67289-8
15. Durak-Kozica M, Baster Z, Kubat K, Stępień E (2018) 3D visualization of extracellular vesicle uptake by endothelial cells. Cell Mol Biol Lett 23:57. https://doi.org/10.1186/s11658-018-0123-z
16. Heusermann W, Hean J, Trojer D, Steib E, von Bueren S, Graff-Meyer A, Genoud C, Martin K, Pizzato N, Voshol J, Morrissey DV, Andaloussi SE, Wood MJ, Meisner-Kober NC (2016) Exosomes surf on filopodia to enter cells at endocytic hot spots, traffic

within endosomes, and are targeted to the ER. J Cell Biol 213(2):173–184. https://doi.org/10.1083/jcb.201506084

17. Tian T, Zhu YL, Zhou YY, Liang GF, Wang YY, Hu FH, Xiao ZD (2014) Exosome uptake through clathrin-mediated endocytosis and macropinocytosis and mediating miR-21 delivery. J Biol Chem 289(32):22258–22267. https://doi.org/10.1074/jbc.M114.588046
18. Treps L, Edmond S, Harford-Wright E, Galan-Moya EM, Schmitt A, Azzi S, Citerne A, Bidère N, Ricard D, Gavard J (2016) Extracellular vesicle-transported Semaphorin3A promotes vascular permeability in glioblastoma. Oncogene 35(20):2615–2623. https://doi.org/10.1038/onc.2015.317
19. Jeon HM, Shin YJ, Lee J, Chang N, Woo DH, Lee WJ, Nguyen D, Kang W, Cho HJ, Yang H, Lee JK, Sa JK, Lee Y, Kim DG, Purow BW, Yoon Y, Nam DH, Lee J (2023) The semaphorin 3A/neuropilin-1 pathway promotes clonogenic growth of glioblastoma via activation of TGF-β signaling. JCI insight 8(21):e167049. https://doi.org/10.1172/jci.insight.167049
20. Tamborini, M., Ribecco, V., Stanzani, E., Sironi, A., Tambalo, M., Franzone, D.,Florio, E., Fraviga, E., Saulle, C., Gagliani, M. C., Pizzocri, M., Mattioli, M.,Cortese, K., Jiang, J. X., Martano, G., Politi, L. S., Riva, M., Pessina, F., Pozzi,D., Lodato, S., ... Matteoli, M. (2025). Extracellular Vesicles Released by Glioblastoma Cancer Cells Drive Tumor Invasiveness via Connexin-43 Gap Junctions. Neuro-oncology,noaf013. Advance online publication. https://doi.org/10.1093/neuonc/noaf013
21. Lucero R, Zappulli V, Sammarco A, Murillo OD, Cheah PS, Srinivasan S, Tai E, Ting DT, Wei Z, Roth ME, Laurent LC, Krichevsky AM, Breakefield XO, Milosavljevic A (2020) Glioma-Derived miRNA-Containing Extracellular Vesicles Induce Angiogenesis by Reprogramming Brain Endothelial Cells. Cell Rep 30(7):2065–2074e4. https://doi.org/10.1016/j.celrep.2020.01.073
22. Giusti I, Monache D, Di Francesco S, Sanità M, D'Ascenzo P, Gravina S, Festuccia GL, C., Dolo V (2016) From glioblastoma to endothelial cells through extracellular vesicles: messages for angiogenesis. Tumour biology: J Int Soc Oncodevelopmental Biology Med 37(9):12743–12753. https://doi.org/10.1007/s13277-016-5165-0
23. Yang ZJ, Bi QC, Gan LJ, Zhang LL, Wei MJ, Hong T, Liu R, Qiu CL, Han XJ, Jiang LP (2022) Exosomes Derived from Glioma Cells under Hypoxia Promote Angiogenesis through Up-regulated Exosomal Connexin 43. Int J Med Sci 19(7):1205–1215. https://doi.org/10.7150/ijms.71912
24. Monteforte A, Lam B, Sherman MB et al (2017) Glioblastoma Exosomes for Therapeutic Angiogenesis in Peripheral Ischemia. Tissue Eng Part A 23(21–22):1251–1261. 10.1089/ten.TEA.2016.0508
25. Rohlenova K, Veys K, Miranda-Santos I, De Bock K, Carmeliet P (2018) Endothelial Cell Metabolism in Health and Disease. Trends Cell Biol 28(3):224–236.

https://doi.org/10.1016/j.tcb.2017.10.010
26. Wang J, Chen Y, Chen S, Mu Z, Chen J (2025) How endothelial cell metabolism shapes blood-brain barrier integrity in neurodegeneration. Front Mol Neurosci 18:1623321 Published 2025 Jun 25. 10.3389/fnmol.2025.1623321
27. Nagy JA, Senger DR (2006) VEGF-A, cytoskeletal dynamics, and the pathological vascular phenotype. Exp Cell Res 312(5):538–548. https://doi.org/10.1016/j.yexcr.2005.10.017

Figures

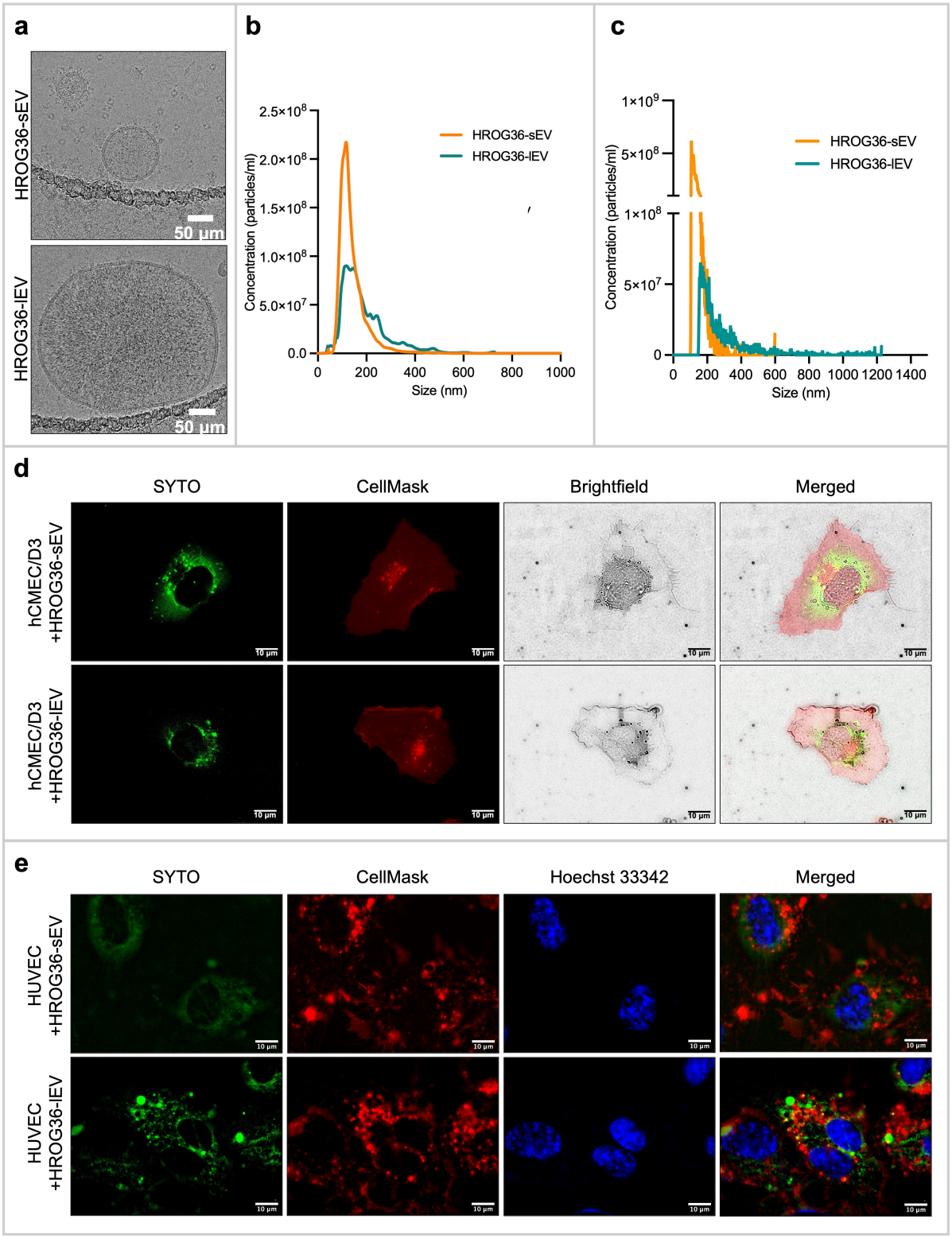


Figure 1

EV Characterisation and Internalisation. **(a)** Representative cryo-TEM images of sEV and lEV. **(b)** EV size distribution assessed by NTA, and **(c)** by TRPS. **(d)** Representative fluorescence microscopy images showing internalisation of fluorescently labelled HROG36-derived sEV and lEV by hCMEC/D3 and **(e)** by HUVEC cells after treatment. EVs were labelled with SYTO RNASelect (green), whereas the cells were stained with CellMask

(red), and nuclei were counterstained with Hoechst 33342 (blue). Merged images show vesicle uptake and cytoplasmic distribution after 24 h of treatment.

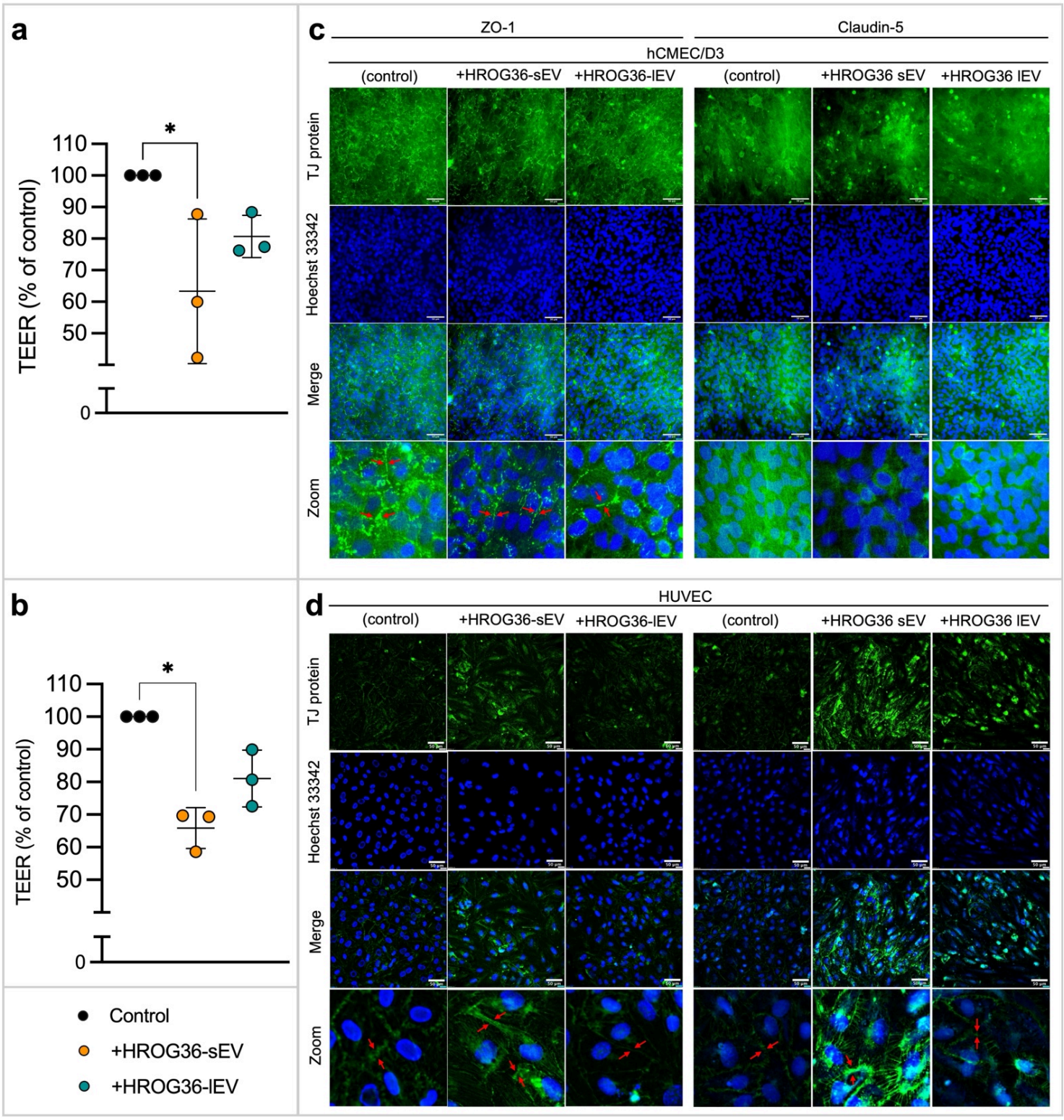


Figure 2

TEER and Localisation of ZO-1 and Claudin-5. TEER measurements of **(a)** hCMEC/D3 and **(b)** HUVEC monolayers after 72 h of treatment with sEV and lEV. Data are presented as normalised percentages relative to the untreated control. Statistical significance was

determined using a nonparametric Kruskal–Wallis test, with $p < 0.05$ considered significant. **(c)** Immunofluorescence staining of expression and localisation of TJ proteins ZO-1 and Claudin-5 in hCMEC/D3 and **(d)** in HUVECs. Cells were stained with ZO-1 or claudin-5 (green) and counterstained with Hoechst 33342 (blue). Red arrows indicate cell borders.

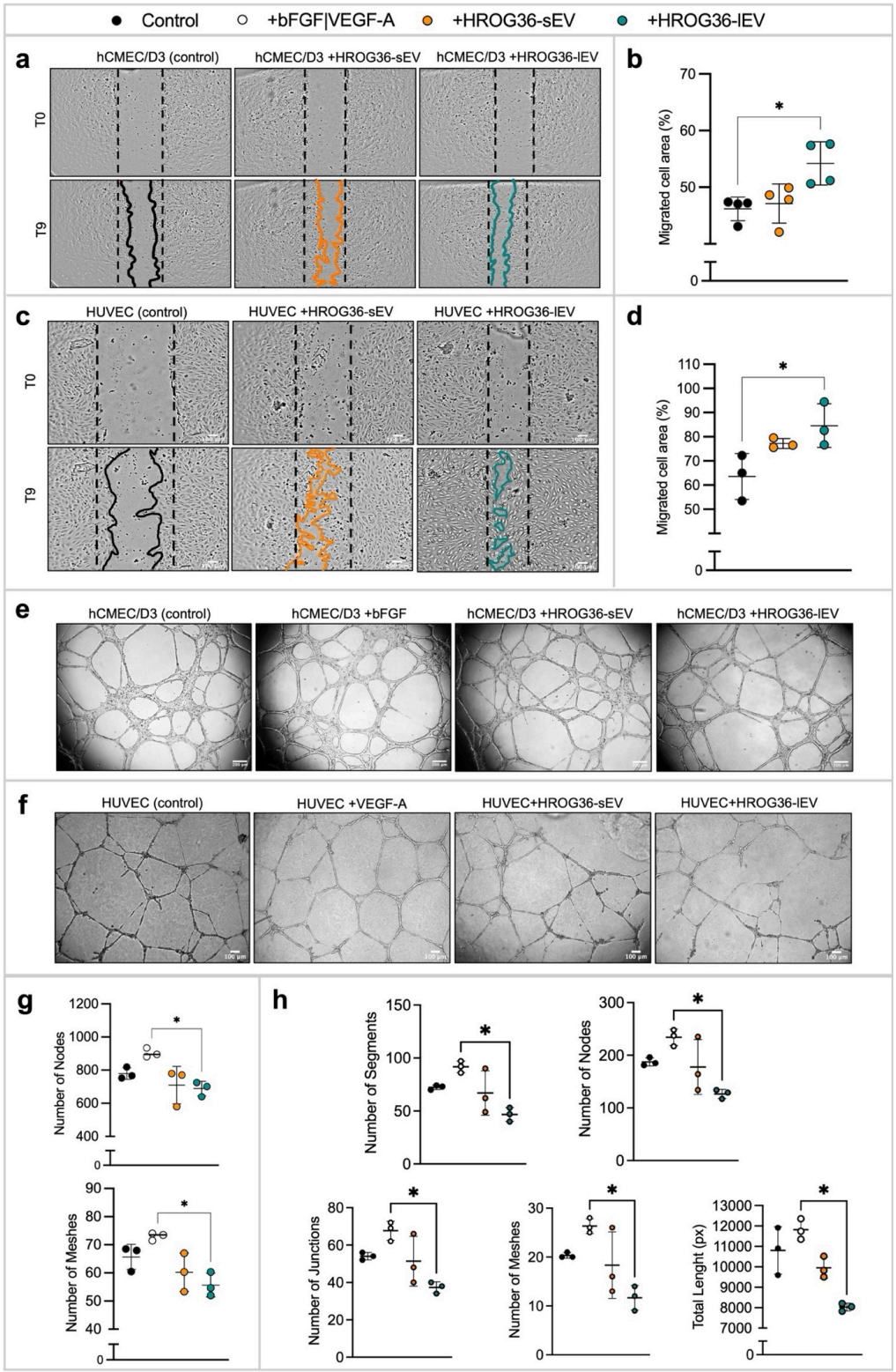


Figure 3

Migration and Tube formation. **(a)** Representative phase-contrast images of hCMEC/D3 monolayers at T0 and T9 for control, sEV-, and lEV-treated cells, and **(c)**HUVEC monolayers under the same conditions. **(b)** Quantification of hCMEC/D3 and **(d)** HUVEC cell migration after treatment with sEV and lEV using the wound-healing assay. The percentage of the area covered by migrated cells was calculated from images acquired at T0 and T9 (9 h post-incubation). **(e)** Representative phase-contrast images of capillary-like networks formed by hCMEC/D3 cells after 24 hours and **(f)** HUVECs after 4 hours. **(g)**Quantitative analysis of hCMEC/D3 and **(h)** HUVEC capillary-like network formation. Quantitative data are presented as mean ± SD from 3-4 independent experiments. Statistical significance was determined using a nonparametric Kruskal–Wallis test, with $p < 0.05$ considered significant.

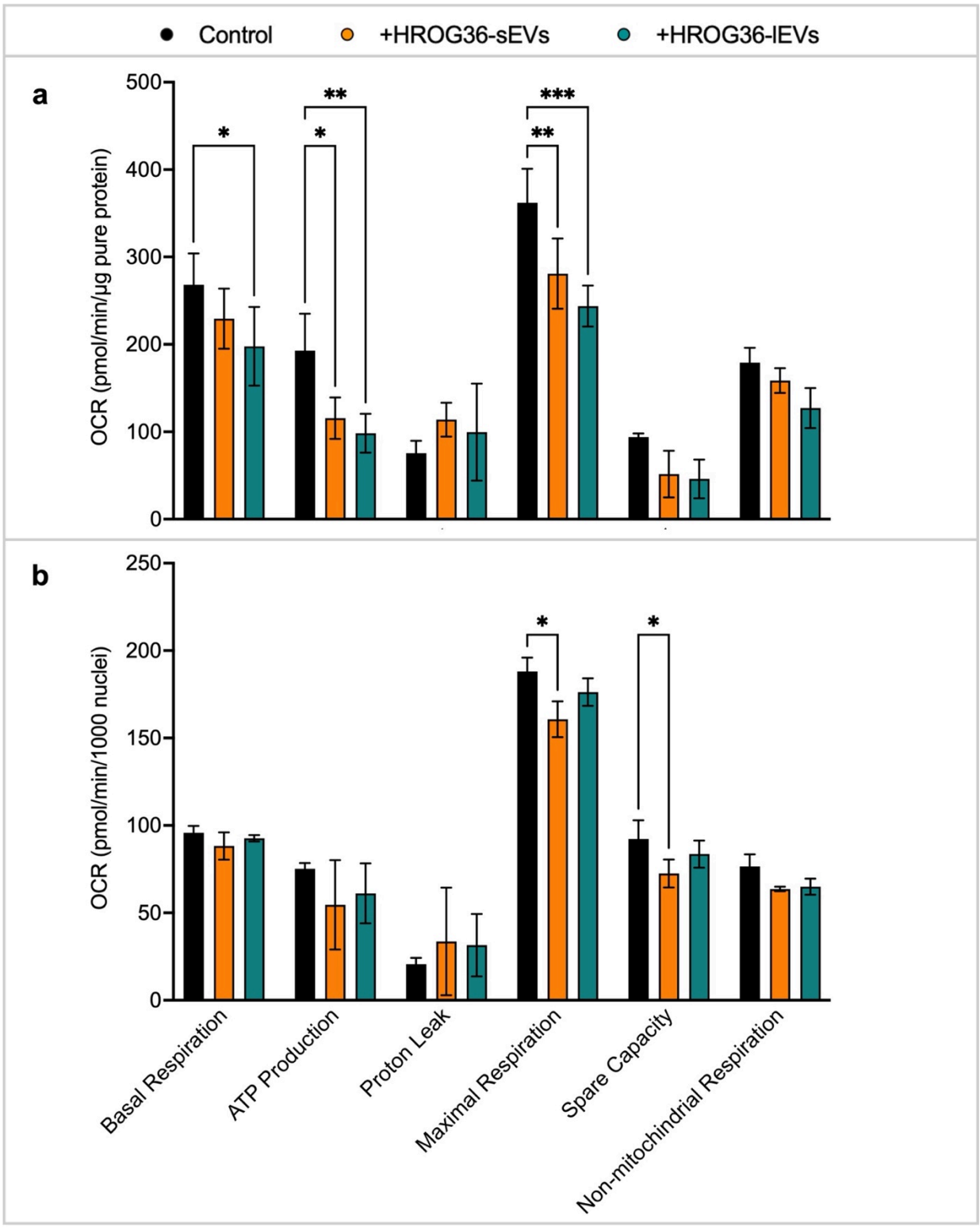


Figure 4

Mitochondrial respiration. Summarized oxygen consumption rate (OCR) parameters in **(a)** hCMEC/D3 and **(b)**HUVEC cells after 72 h treatment with HROG36-derived sEV or lEV. Quantitative data are presented as mean ± SD from 3 independent experiments. Statistical significance was evaluated using two-way ANOVA followed by Dunnett's multiple

comparisons test. *p < 0.05, **p < 0.01, and **p < 0.001 were considered statistically significant.

Supplementary Files

This is a list of supplementary files associated with this preprint. Click to download.

- GA.png